## nature nanotechnology

**Article** 

https://doi.org/10.1038/s41565-022-01264-4

# Real-space nanoimaging of hyperbolic shear polaritons in a monoclinic crystal

Received: 10 May 2022

Accepted: 14 October 2022

Published online: 12 December 2022

Check for updates

Guangwei Hu (\$\mathbf{0}^{1,12}\$, Weiliang Ma<sup>2,12</sup>, Debo Hu (\$\mathbf{0}^{3,12}\$, Jing Wu<sup>4</sup>, Chunqi Zheng<sup>1,5</sup>, Kaipeng Liu<sup>1</sup>, Xudong Zhang<sup>6</sup>, Xiang Ni<sup>7</sup>, Jianing Chen<sup>8</sup>, Xinliang Zhang<sup>2</sup>, Qing Dai (\$\mathbf{0}^{3}\subseteq\$), Joshua D. Caldwell (\$\mathbf{0}^{9}\$, Alexander Paarmann (\$\mathbf{0}^{10}\$), Andrea Alù (\$\mathbf{0}^{7,11}\subseteq\$), Peining Li (\$\mathbf{0}^{2}\subseteq\$ & Cheng-Wei Qiu (\$\mathbf{0}^{1,5}\subseteq\$)

Various optical crystals possess permittivity components of opposite signs along different principal directions in the mid-infrared regime, exhibiting exotic anisotropic phonon resonances. Such materials with hyperbolic polaritons—hybrid light-matter quasiparticles with open isofrequency contours—feature large-momenta optical modes and wave confinement that make them promising for nanophotonic on-chip technologies. So far, hyperbolic polaritons have been observed and characterized in crystals with high symmetry including hexagonal (boron nitride), trigonal (calcite) and orthorhombic ( $\alpha$ -MoO<sub>3</sub> or  $\alpha$ -V<sub>2</sub>O<sub>5</sub>) crystals, where they obey certain propagation patterns. However, lower-symmetry materials such as monoclinic crystals were recently demonstrated to offer richer opportunities for polaritonic phenomena. Here, using scanning near-field optical microscopy, we report the direct real-space nanoscale imaging of symmetry-broken hyperbolic phonon polaritons in monoclinic CdWO<sub>4</sub> crystals, and showcase inherently asymmetric polariton excitation and propagation associated with the nanoscale shear phenomena. We also introduce a quantitative theoretical model to describe these polaritons that leads to schemes to enhance crystal asymmetry via the damping loss of phonon modes. Ultimately, our findings show that polaritonic nanophotonics is attainable using natural materials with low symmetry, favouring a versatile and general way to manipulate light at the nanoscale.

Optical anisotropic behaviours are an important feature of natural optical materials in the context of crystal optics¹. Recently, extreme optical anisotropy—in the form of hyperbolic responses—has been identified in various polar crystals, for which the permittivity components along different principal directions of the crystals show different signs. When interacting with light, such polar materials may yield hyperbolic phonon polaritons, that is, quasiparticles of coupled light and infrared-active optical phonons with hyperbolic dispersion²-6. Various materials supporting this response have been studied, from van der Waals thin films6 including hexagonal boron nitride (hBN) $^{7-9}$ , alpha-phase molybdenum trioxide ( $\alpha$ -MoO $_3$ ) $^{10-12}$  and its twisted bilayers $^{12-14}$ , alpha-phase vanadium

pentoxide  $(\alpha \cdot V_2 O_5)^{15}$ , and anisotropic bulk crystals such as calcite  $^{16}$  and  $\beta$ -gallium oxide  $^{17,18}$ . These polaritons exhibit low loss  $^{19}$  and strong wave confinement associated with their large momenta  $^{20,21}$ , thus enhancing light–matter interactions  $^{22,23}$  and allowing the directional control of energy flow  $^{24}$  at the nanoscale for applications such as infrared sensing  $^{25,26}$ , subdiffractive imaging  $^{8,9,27}$  and photodetection  $^{28}$ , to name a few.

In crystallography, most of these anisotropic media are categorized as hexagonal (hBN; Fig. 1a), trigonal (calcite, rhombohedral) and orthorhombic ( $\alpha$ -V<sub>2</sub>O<sub>5</sub>,  $\alpha$ -MoO<sub>3</sub>; Fig. 1b) crystals. They demonstrate higher symmetry compared with low-symmetry crystals (LSCs) such as monoclinic (Fig. 1c) and triclinic lattices<sup>29,30</sup>. Monoclinic crystals,

A full list of affiliations appears at the end of the paper. Ze-mail: daig@nanoctr.cn; aalu@gc.cuny.edu; lipn@hust.edu.cn; chengwei.qiu@nus.edu.sg

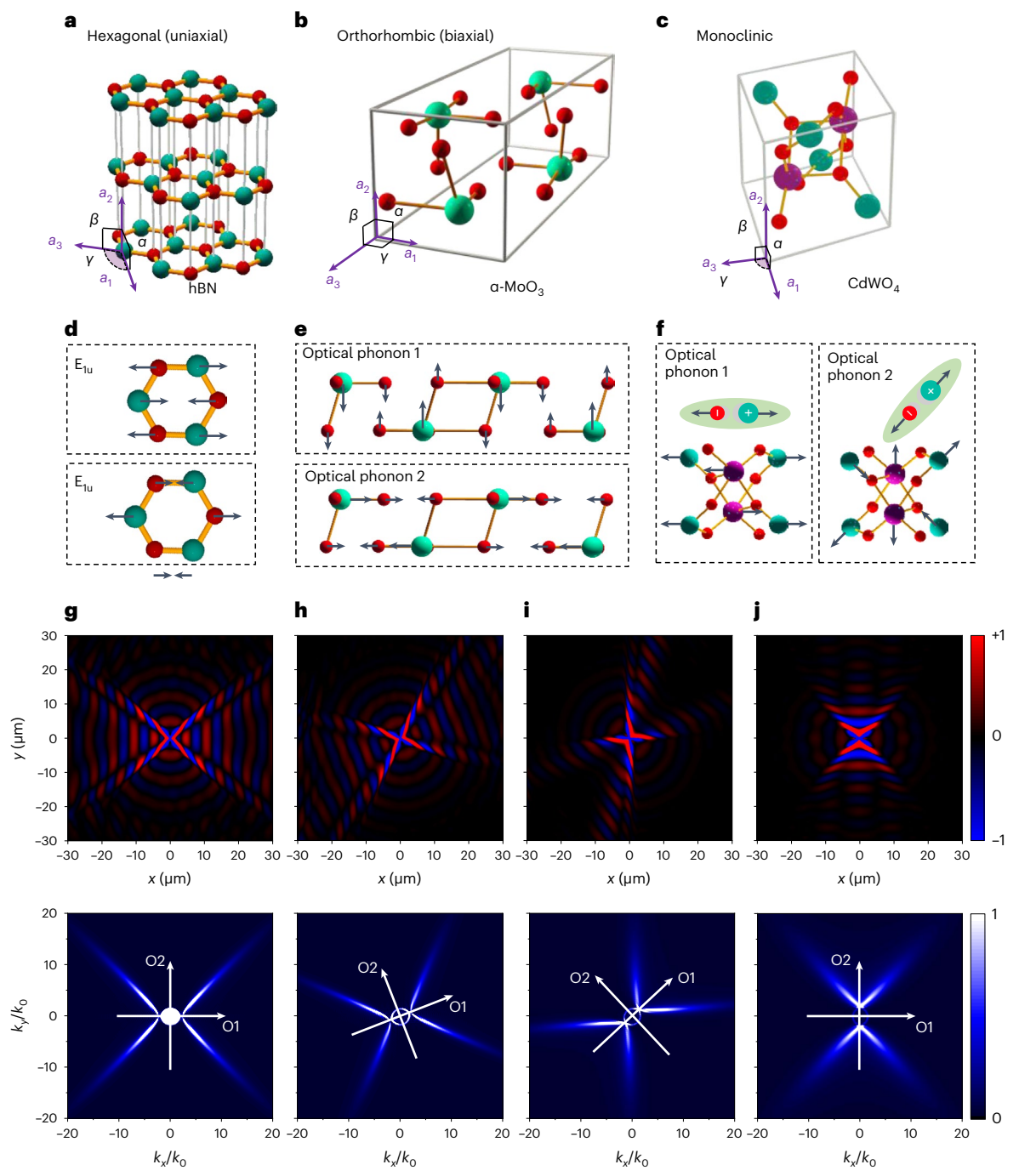


**Fig. 1**| **Hyperbolic polaritons in LSCs. a**, Hexagonal crystal in an example of hBN with uniaxial optical property. **b**, Orthorhombic α-MoO<sub>3</sub> crystal featuring the biaxial optical property. **c**, Monoclinic CdWO<sub>4</sub> crystal with lower symmetry. Here three parameters  $\mathbf{a}_1$ ,  $\mathbf{a}_2$  and  $\mathbf{a}_3$  denote vectors of the unit cell, where the angle between them are  $\alpha = \langle \mathbf{a}_1, \mathbf{a}_2 \rangle$ ,  $\beta = \langle \mathbf{a}_2, \mathbf{a}_3 \rangle$  and  $\gamma = \langle \mathbf{a}_1, \mathbf{a}_3 \rangle$ . **d**, Eigendisplacement of degenerate  $E_{1u}$  phonon resonance in hexagonal crystals. **e**, The two eigendisplacements of ions for two transverse optical phonons in the orthorhombic crystal, which are orthogonal. **f**, Schematic of the

eigendisplacement for two non-degenerate transverse optical phonons in the LSC. They, in general, can induce two non-orthogonal dipolar resonance (inset). Here the black arrow denotes the displacement.  ${\bf g}$ - ${\bf j}$ . Numerical field distribution (Re[ $F_z$ ], top rows) and its corresponding hyperbolic dispersion (fast Fourier transform (FFT), bottom rows) in the LSC. Here we vary the angle between the two non-degenerate transverse optical resonances to be  $0^{\circ}$  ( ${\bf g}$ ),  $30^{\circ}$  ( ${\bf h}$ ),  $60^{\circ}$  ( ${\bf i}$ ) and  $90^{\circ}$  ( ${\bf j}$ ). The working frequency is 870 cm $^{-1}$ . The white lines with arrows show the directions of the effective optical axis.

in particular, are characterized by unequal lengths of their three principal axes. In addition, they support only two-fold axis of rotational symmetry along  $\mathbf{a}_2$  and a mirror plane ( $\mathbf{a}_1$ – $\mathbf{a}_3$  plane), but their  $\mathbf{a}_1$  and  $\mathbf{a}_3$  axes are non-orthogonal (Fig. 1c). Such reduced symmetry introduces challenges for some optical applications, but at the same time offers an interesting 'knob' for fine phase and polarization control of light propagation<sup>17</sup>. The impact of the low structural symmetry on the polaritonic

response at the deeply subwavelength scale has only recently been investigated, resulting in the observation of so-called shear polaritons, where both momentum (wavelength) and propagation direction disperse with frequency<sup>18</sup>. Nevertheless, a direct real-space observation of polariton propagation in LSCs as well as full modelling of exotic surface modes could complement the understanding of the impact of such low symmetry on polariton propagation.

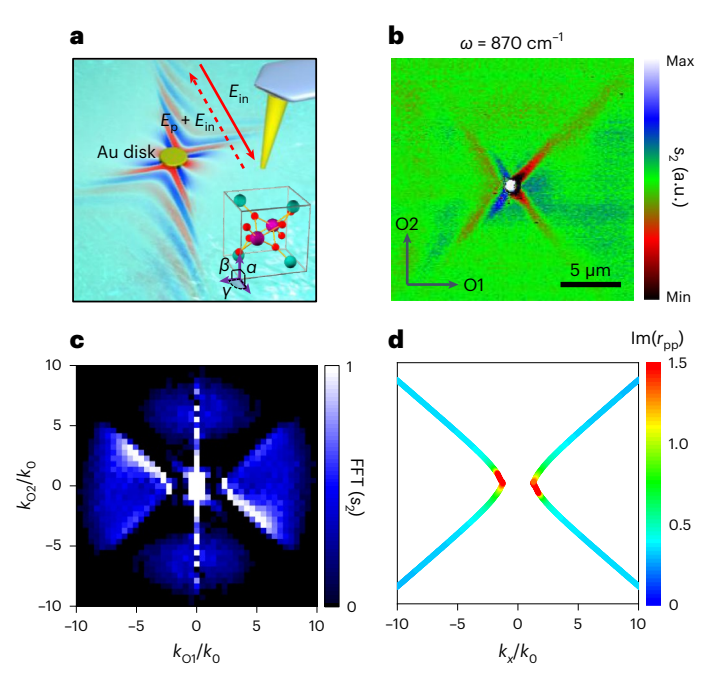


**Fig. 2** | **Near-field observation of polaritons in LSCs. a**, Schematic of scattering type near-field mapping of hyperbolic phonon polaritons in CdWO<sub>4</sub>. The crystal structure is shown in the inset. The Au disc serves as the nanoantenna to launch the polaritons, whereas the tip records the Au-launched polariton ( $E_p$ ) as well as the incident light ( $E_{\rm in}$ ). **b**, Measured near-field signals at the surface of CdWO<sub>4</sub> at frequency  $\omega$  = 870 cm<sup>-1</sup>. Here the lab coordinate is denoted as O1 and O2, the direction of the two effective optic axis. **c**, Corresponding Fourier spectrum of the measured near-field signals in **b**. **d**, Calculated dispersion characterized by the imaginary part of the reflection coefficient.

In this paper, we discuss the role of lower crystal symmetry on the generation and propagation of hyperbolic shear phonon polaritons, and report their near-field real-space observation in monoclinic cadmium tungstate (CdWO<sub>4</sub>), an LSC well known for its application in scintillation detectors  $^{31}$ . The real-space nanoimaging of polaritons at the surface of CdWO<sub>4</sub> is achieved by scattering-type scanning near-field optical microscopy (s-SNOM), revealing open polariton wavefronts with asymmetric propagation signatures. Such asymmetry fundamentally originates from the fact that the non-Hermitian permittivity tensor cannot be diagonalized in real space as interpreted by our theory (Supplementary Section 1). Our results suggest that LSCs naturally facilitate additional degrees of freedom to mould the interfacial flow of light at the nanoscale.

# Impact of crystal symmetry on the optical response

A crystal with a hexagonal lattice supports degenerate optical phonons oscillating in the plane, which implies the presence of in-plane isotropic polariton propagation in hBN (refs. 7-9) (Fig. 1d). For orthorhombic lattices, non-degenerate dipolar excitations of phonon resonances can exist with different strengths due to inequal lattice constants, thus offering in-plane anisotropy in  $\alpha$ -MoO<sub>3</sub> (refs. <sup>10,11</sup>) and  $\alpha$ -V<sub>2</sub>O<sub>5</sub> (ref. <sup>15</sup>) (Fig. 1e). In contrast, multiple dipolar excitations in the form of optical phonons in LSCs will not necessarily be orthogonal to one another (Fig. 1f), due to the low crystal symmetry and anharmonic lattice vibrations<sup>32</sup>. To consider the dielectric response of optical crystals, each optical phonon mode contributes to the permittivity tensor as a Lorentzian oscillator (denoted as  $\varphi_l$ , where subscript integer l denotes the mode index) with the auxiliary freedom of their angular orientation  $(y_i)$ (Methods). Here, due to the orthogonality of phonon modes in hexagonal, trigonal and orthorhombic crystals,  $\gamma_i$  is either 0° or 90°, which is usually overlooked. However, in LSCs,  $\gamma_i$  can be nearly arbitrary, offering a new degree of freedom for controlling the optical response and light propagation. Hence, four independent components of the permittivity tensor arise in monoclinic LSCs. written in Cartesian coordinates as

$$\bar{\bar{\varepsilon}} = \begin{bmatrix} \varepsilon_{xx} & \varepsilon_{xy} & 0 \\ \varepsilon_{yx} & \varepsilon_{yy} & 0 \\ 0 & 0 & \varepsilon_{zz} \end{bmatrix},$$
(1)

where  $\varepsilon_{xy} = \varepsilon_{yx}$  is bounded by reciprocity. Since all these dispersive components are complex-valued entries, this is a non-Hermitian tensor<sup>17</sup>. Importantly, when  $\overline{\varepsilon}$  is non-diagonalizable in real space using unitary rotation matrices, we could obtain the symmetry breaking of polaritons (Methods and Supplementary Sections 1 and 2).

To directly visualize the effect of this lower symmetry on the nanoscale propagation of light, we first consider a crystal with two non-orthogonal, non-degenerate (that is, different oscillation eigenfrequencies) optical phonons with different orientations (with angle  $\Delta y = y_2 - y_1$ , where  $y_1$  is 0 for the sake of simplicity here; Supplementary Section 1) and performed full-wave numerical finite element simulations to examine dipole-launched polaritonic modes (Methods). We fixed the frequency at 870 cm<sup>-1</sup>. The field at the top surface of the  $\mathbf{a}_1 - \mathbf{a}_3$ plane is shown in Fig. 1g-j. When  $\Delta y = 0^{\circ}$  (Fig. 1g) or  $\Delta y = 90^{\circ}$  (Fig. 1j), the polaritons at the interface are symmetric with respect to two optic axes (along the x and y directions), showing hyperbolic dispersion in the Fourier spectrum (Fourier transform of the field). However, for different angles, we find asymmetric propagation of polaritons with respect to the effective optic axis and different open directions when  $\Delta y = 30^{\circ}$  (Fig. 1h), which becomes more pronounced when  $\Delta y = 60^{\circ}$ (Fig. 1i). Here the two effective optic axis (O1 and O2) are in the plane and along the directions where the real part of permittivity tensor can be diagonalized (Supplementary Section 1), which provides the symmetric responses if loss is neglected. The fundamental mechanism is the excitation of asymmetric hyperbolic polaritons, as shown in their Fourier transform spectrum, due to the non-orthogonality of the two underlying phonon modes, which will be discussed in more detail later. This evidence points to the fact that LSCs offer a new platform for the extreme manipulation of the flow of polaritons and energy.

# Real-space nanoimaging of hyperbolic shear polaritons

To map such an asymmetric dispersion of hyperbolic shear phonon polaritons, we performed s-SNOM at the (010) surface of a CdWO<sub>4</sub> crystal. The CdWO<sub>4</sub> crystal has monoclinic symmetry with space group 13 (P12/C1), which supports eight optically active non-orthogonal optical phonons ( $B_u$  symmetry) with polarization in the  $\mathbf{a}_1$ - $\mathbf{a}_3$  plane and seven phonon modes ( $A_{ij}$  symmetry) with polarization along the  $\mathbf{a}_2$ direction<sup>32</sup>. We denote the orientation angles of the induced polarization as  $y_l$  (l = 1, 2, .... 8 from high to low frequency), all of which are different (see the specific values provided in the table in Supplementary Section 1). In our sample, the eigendisplacements of the optical phonons of interest are within the CdWO<sub>4</sub>/air interface, which is ideal for s-SNOM nanoimaging. We define the x direction as parallel to the  $\mathbf{a}_1$  axis of the crystal unit cell and the normal direction of this interface as z (which is parallel to the  $\mathbf{a}_2$  direction). The sample thickness is 5 mm with surface dimensions of  $5 \times 5$  mm<sup>2</sup>, much larger than the operating wavelength of interest. Thus, we can reasonably regard the sample to be semi-infinite. We fabricated gold (Au) discs (diameter,  $\sim$ 1  $\mu$ m) on the surface of CdWO<sub>4</sub>. As shown in Fig. 2a, when illuminating a laser beam with p-polarized mid-infrared light onto the disc  $(E_{in})$ , it will act as an optical antenna launching polaritons  $(E_p)$  propagating along the surface, which would be picked up by the tip of s-SNOM. Note that we effectively align the illumination direction along the O1 axis (with an incident angle of 30°) to avoid any illumination-caused asymmetry in the direction parallel to the O2 axis.

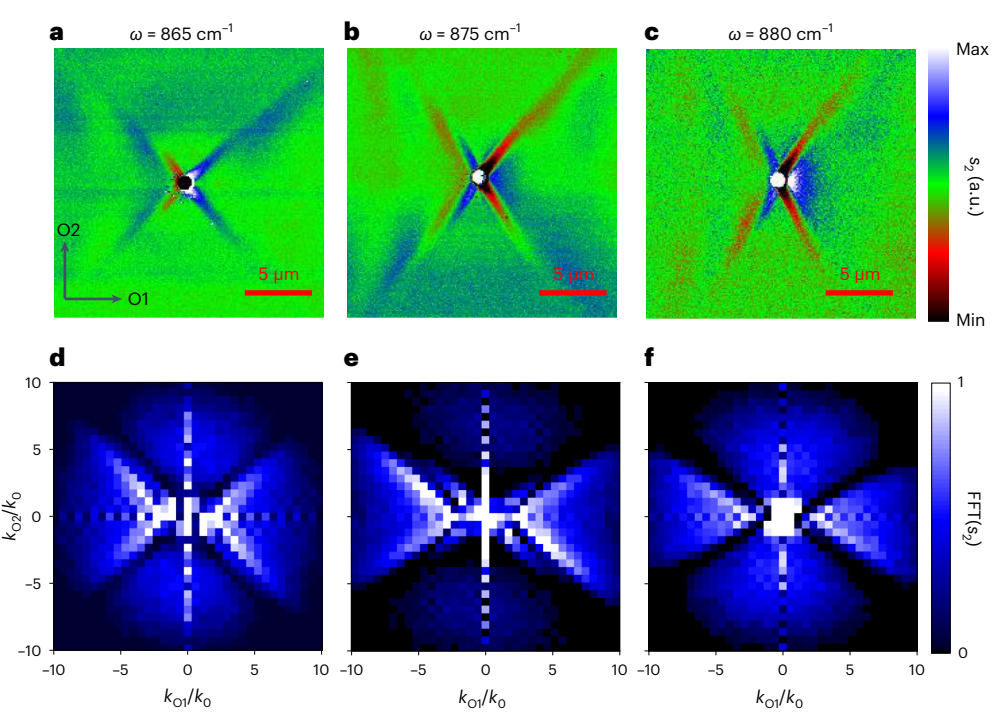


**Fig. 3** | **Near-field images of polaritons in low-symmetry CdWO<sub>4</sub> crystals.**  $\mathbf{a}$ - $\mathbf{c}$ , Measured near-field signals at the surface of CdWO<sub>4</sub> at frequency  $\omega = 865 \, \mathrm{cm}^{-1}$  (**a**),  $\omega = 875 \, \mathrm{cm}^{-1}$  (**b**) and  $\omega = 880 \, \mathrm{cm}^{-1}$  (**c**).  $\mathbf{d}$ - $\mathbf{f}$ , Fourier spectrum of the measured signals corresponding to the data in a (**d**), b (**e**) and c (**f**). All of them exhibit the robust feature of asymmetric propagation of hyperbolic shear polaritons.

For our experimental measurements, we focus on phonon polaritons in the infrared Reststrahlen band (RB) within the spectral range from 780 to 901 cm<sup>-1</sup> (as limited by our laser source in the experimental setup), whereas other optical phonons-neither orthogonal nor parallel to these phonons—and the induced polarization from the  $\bar{\varepsilon}_{\infty}$  term contribute to the asymmetry (Supplementary Section 1 and Supplementary Fig. 5). The near-field amplitude image at  $\omega = 870 \text{ cm}^{-1}$  is presented in Fig. 2b, showing long (over 5 µm) and ray-like polariton propagation. The Fourier spectrum of the near-field images is exhibited in Fig. 2c, demonstrating in-plane hyperbolic characteristics. These observations agree well with the numerical simulations (Supplementary Fig. 6), verifying the in-plane hyperbolic responses of CdWO<sub>4</sub> polaritons and suggesting the capability of the strong confinement of light at the nanoscale due to the unbounded open dispersion contours. We attribute the vertical bright lines in the Fourier spectrum to noise.

More important is that the observed polariton patterns are asymmetric with respect to both O1 and O2 axes. We attribute the asymmetry with respect to O2 axis to the oblique illumination<sup>33</sup>, similar to the recent experimental observation of polaritons in calcite<sup>10</sup>. Interestingly, an additional asymmetry with respect to the O1 axis is observed: the polaritonic rays notably decay faster on the upper right side of the O1 axis than to the lower right side (Fig. 2b; Supplementary Fig. 7 shows the analysis of line-cut signals). Such asymmetry is absent in calcite polaritons because the mirror symmetry in trigonal crystals guarantees the symmetric excitation of polaritons with respect to the plane containing the optic axis and normal direction of the interface. Hence, our observed symmetry breaking with respect to the O1 axis is an intrinsic property of LSC with broken mirror symmetry and hence independent of illumination, because we fixed the illumination direction in the measurements to be parallel to the O1 axis. The asymmetry is also reflected in the Fourier transform analysis of the near-field images (Fig. 2c), namely, when  $k_{O1} > 0$ , the upper isofrequency curve  $(k_{O2} > 0)$  is shorter than the lower branch  $(k_{02} < 0)$ . These landmark observations support that monoclinic CdWO<sub>4</sub> can indeed render the low-symmetry polaritons, predicted by

our theoretical calculation of dispersion (Fig. 2d and Supplementary Fig. 8), which will be discussed in detail later.

Such asymmetric propagation of polaritons is robust; to confirm this feature, we measured the polaritons at other frequencies including  $\omega = 865 \text{ cm}^{-1} \text{ (Fig. 3a)}, \omega = 875 \text{ cm}^{-1} \text{ (Fig. 3b)} \text{ and } \omega = 880 \text{ cm}^{-1} \text{ (Fig. 3c)}.$ The corresponding Fourier spectra are shown in Fig. 3d-f, respectively, all of which exhibit asymmetry. Although these measurements are in the same RB, we note that asymmetric hyperbolic polaritons are predicted to also arise in other RBs, as shown in the theoretical calculations in Supplementary Figs. 4 and 5. In addition, the open direction of hyperbolic dispersion changes with respect to the operation frequency in different RBs (numerical and experimental demonstrations are provided in Supplementary Section 1 and Supplementary Figs. 2 and 3), and sometimes even noticeable within the same RB (Supplementary Figs. 4 and 5). To summarize, the extreme anisotropy, symmetry breaking and dispersion of optic axis are three distinguishing features of LSC, which are unattainable in tetragonal, trigonal, hexagonal or orthorhombic systems with higher symmetry.

# Quantitative measurement and physical origins of hyperbolic shear polaritons

The demonstrated symmetry breaking can be further enhanced. Polariton asymmetry essentially stems from the non-diagonalizability of a complex permittivity tensor in real space <sup>17</sup> due to non-orthogonal phonon modes (Fig. 1) and attested by our experiments. It is worth noting that the damping loss of each individual mode plays an important role, as it can modify the extent of how such complex permittivity tensor deviates from being diagonalized in real space. Such derivation is quantitatively measured as an  $\mathcal M$  value, where a larger value refers to lower symmetry (Methods and Supplementary Section 2). We, thus, start from the case study shown in Fig. 1i, which corresponds to the orientation angle  $\Delta \gamma = 60^\circ$  and frequency  $\omega = 870$  cm<sup>-1</sup>, and alter  $\mathcal M$  by tuning the damping loss of one phonon mode ( $S_1$ ) to check how the polariton asymmetry will change. We performed numerical simulations using a dipole to excite the hyperbolic shear polaritons in the crystal

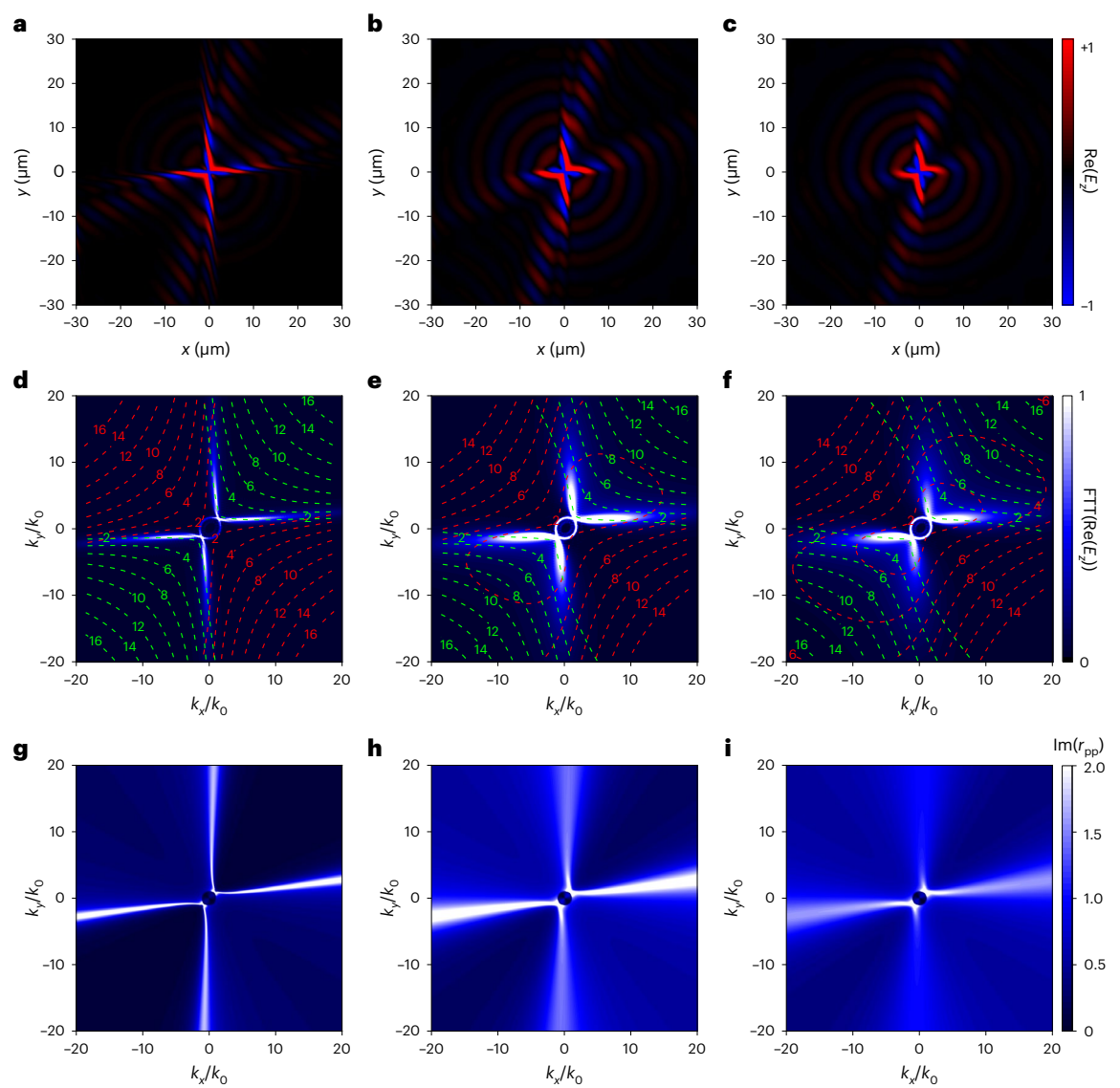


**Fig. 4** | **Symmetry-broken nature of hyperbolic polaritons in LSCs. a**-c, Field distribution, that is, real part of  $E_z[\text{Re}(E_z)]$ , of the dipole-launched polaritons at the 20 nm top of the materials at 870 cm<sup>-1</sup>. Here the permittivity tensor is obtained using two non-degenerate optical phonons, as the damping (*S*) of one mode is varied:  $S_1 = 10 \text{ cm}^{-1}(\mathbf{a})$ ,  $S_1 = 30 \text{ cm}^{-1}(\mathbf{b})$  and  $S_1 = 50 \text{ cm}^{-1}(\mathbf{c})$ .  $\mathbf{d}$ - $\mathbf{f}$ . Fourier spectra of the field distribution, that is, FFT[Re( $E_z$ )] for  $\mathbf{a}$  ( $\mathbf{d}$ ),  $\mathbf{b}$  ( $\mathbf{e}$ ) and  $\mathbf{c}$  ( $\mathbf{f}$ ).

The red and green dashed contour lines mean the real and imaginary parts of momentum along the z direction  $(k_z)$ , respectively, at the associated position of  $(k_x, k_y)$ ,  $\mathbf{g}$ - $\mathbf{i}$ , Calculated dispersion of the resonant mode at the surface for  $\mathbf{a}$  ( $\mathbf{g}$ ),  $\mathbf{b}$  ( $\mathbf{h}$ ) and  $\mathbf{c}$  ( $\mathbf{i}$ ). Here the colour bar is the imaginary part of reflection, that is,  $\mathrm{Im}(r_{\mathrm{pp}})$ , of the transverse-magnetic polarized (denoted as 'p') component at the transverse-magnetic polarized incidence.

and rigorously derive the dispersion of the polariton modes. The numerical field distribution is shown in Fig. 4a–c, in which three different damping levels are considered:  $S_1$  = 10 cm<sup>-1</sup> ( $\mathcal{M}$  = 0.0011; Fig. 4a),  $S_1$  = 30 cm<sup>-1</sup> ( $\mathcal{M}$  = 0.0263; Fig. 4b) and  $S_1$  = 50 cm<sup>-1</sup> ( $\mathcal{M}$  = 0.0808; Fig. 4c). Evidently, the field distribution becomes increasingly asymmetric with respect to the O1 axis, in accordance with their Fourier spectra (Fig. 4d–f). Besides, since we have  $\mathcal{M}$  = 0.0186 (Fig. 1i), we indeed can visualize that the asymmetry in Fig. 4b,c is stronger than that in Fig. 1i, whereas the asymmetry in Fig. 4a is weaker than that in Fig. 1i. These observations suggest a possible route to quantitatively measure the degree of asymmetry with our method. We anticipate that such an avenue to enhance asymmetry can be realized by reducing the isotope purity or increasing the working temperature of LSCs. It may increase the dampings of the associated phonon modes, which could be experimentally explored in the future.

Finally, we discuss the physical origin behind this asymmetry. It is known that resonant modes at the interface correspond to poles of the

dyadic Green's function of the system, which arises when the transverse impedances in the two media are opposite to each other. In our case, we denote the transverse wave impedance of the background isotropic dielectric as  $\eta_d \propto k_z^d$  (where  $k_z^d = \sqrt{\varepsilon_d k_0^2 - k_\rho^2}$  is the momentum along the z direction in the background with dielectric constant  $\varepsilon_d$ ) and in the anisotropic crystal as  $\eta_c \propto \frac{1}{k_z}$  (where  $k_z$  is the momentum along the z direction of optical crystals). The transverse resonance condition requires  $\eta_d + \eta_c = 0$  (a detailed derivation is provided in Supplementary Section 3). Since  $\eta_d$  does not depend on the in-plane direction of interest due to material isotropy, we examine the  $\eta_c$  component. For this purpose, we show the  $k_z$  of the crystal as contour line plots (Fig. 4d-f), where the red and green dashed lines denote Re[ $k_z$ ] and Im[ $k_z$ ], respectively. In Fig. 4d, one can find that the resonant modes and  $k_z$  distribution are nearly symmetric with respect to the O1 axis. However, when the symmetry is broken due to higher damping,

we observe enhanced asymmetry in the dispersion plot of  $k_z$  (Fig. 4e,f). Such distorted momenta suggest an asymmetric transverse resonance at the interface for a particular point in momentum space at which the wave impedance-matching condition is reached; its mirror point with respect to the O1 axis will not satisfy this matching condition due to the asymmetry of the solution for  $k_z$ . As a consequence, the polariton propagation becomes asymmetric on the two sides of the O1 axis (Fig. 4b,c). Our interpretation is further supported by the agreement between the numerically obtained Fourier spectra and our analytical calculations shown in Fig. 4g-i. We note that this asymmetric resonance condition also explains our experimental observation of asymmetric CdWO<sub>4</sub> polaritons, as shown by the different resonant amplitudes of the reflection coefficient (Fig. 2d), which can be further enhanced if the distortion of  $k_z$  is more pronounced (Supplementary Fig. 9). This model is applicable to other scenarios regardless of the material loss and frequency dispersion. Hence, this can be readily extended to other monoclinic crystals and triclinic systems with even lower symmetry.

#### Conclusions

In this work, we studied asymmetric hyperbolic phonon polaritons in LSC with an exemplary monoclinic crystal CdWO $_4$ . Combined with rigorous theoretical investigations, we provided direct real-space nanoimaging of rotating and asymmetric polaritons. Essentially, the reduced symmetry of LSCs stems from the non-diagonalizability of complex permittivity tensors in real space, which renders the distorted dissipation and underpins extreme asymmetric propagation of shear polaritons. Such LSCs, therefore, provide an ideal and naturally occurring paradigm to non-Hermitian photonics. Moreover, the study of natural LSCs will further inspire its meta-photonics and meta-optics  $^{34}$ . Our findings with tailorable symmetry-broken hyperbolic polaritons in bulk crystals will be important and readily valuable for various technologies such as infrared sensing, super-Planckian heat emission, near-field radiation management, photonic circuits and many others.

#### Online content

Any methods, additional references, Nature Research reporting summaries, source data, extended data, supplementary information, acknowledgements, peer review information; details of author contributions and competing interests; and statements of data and code availability are available at https://doi.org/10.1038/s41565-022-01264-4.

#### References

- Born, M. & Wolf, E. Principles of Optics 5th edn, 333–334 (Pergamon, 1975).
- Caldwell, J. D. et al. Low-loss, infrared and terahertz nanophotonics using surface phonon polaritons. *Nanophotonics* 4, 44–68 (2015).
- 3. Basov, D. N., Fogler, M. M. & García de Abajo, F. J. Polaritons in van der Waals materials. *Science* **354**, aag1992 (2016).
- Low, T. et al. Polaritons in layered two-dimensional materials. Nat. Mater. 16, 182–194 (2017).
- Hu, G., Shen, J., Qiu, C.-W., Alù, A. & Dai, S. Phonon polaritons and hyperbolic response in van der Waals materials. Adv. Opt. Mater. 8, 1901393 (2020).
- Zhang, Q. et al. Interface nano-optics with van der Waals polaritons. Nature 597, 187–195 (2021).
- Dai, S. et al. Tunable phonon polaritons in atomically thin van der Waals crystals of boron nitride. Science 343, 1125–1129 (2014).
- Caldwell, J. D. et al. Sub-diffractional volume-confined polaritons in the natural hyperbolic material hexagonal boron nitride. *Nat. Commun.* 5, 5221 (2014).
- Li, P. et al. Hyperbolic phonon-polaritons in boron nitride for near-field optical imaging and focusing. Nat. Commun. 6, 7507 (2015).

- Zheng, Z. et al. Highly confined and tunable hyperbolic phonon polaritons in van der Waals semiconducting transition metal oxides. Adv. Mater. 30. e1705318 (2018).
- 11. Ma, W. et al. In-plane anisotropic and ultra-low-loss polaritons in a natural van der Waals crystal. *Nature* **562**, 557–562 (2018).
- Hu, G. et al. Topological polaritons and photonic magic angles in twisted α-MoO<sub>3</sub> bilayers. *Nature* 582, 209–213 (2020).
- Duan, J. et al. Twisted nano-optics: manipulating light at the nanoscale with twisted phonon polaritonic slabs. *Nano Lett.* 20, 5323–5329 (2020).
- Zheng, Z. et al. Phonon polaritons in twisted double-layers of hyperbolic van der Waals crystals. Nano Lett. 20, 5301–5308 (2020).
- Taboada-Gutiérrez, J. et al. Broad spectral tuning of ultra-low-loss polaritons in a van der Waals crystal by intercalation. *Nat. Mater.* 19, 964–968 (2020).
- Ma, W. et al. Ghost hyperbolic surface polaritons in bulk anisotropic crystals. Nature 596, 362–366 (2021).
- Schubert, M. et al. Anisotropy, phonon modes, and free charge carrier parameters in monoclinic β-gallium oxide single crystals. Phys. Rev. B 93, 125209 (2016).
- Passler, N. et al. Hyperbolic shear polaritons in low-symmetry crystals. Nature 602, 595–600 (2022).
- 19. Giles, A. J. et al. Ultralow-loss polaritons in isotopically pure boron nitride. *Nat. Mater.* **17**, 134–139 (2018).
- Lee, I.-H. et al. Image polaritons in boron nitride for extreme polariton confinement with low losses. *Nat. Commun.* 11, 3649 (2020).
- Ambrosio, A. et al. Selective excitation and imaging of ultraslow phonon polaritons in thin hexagonal boron nitride crystals. *Light* Sci. Appl. 7, 27 (2018).
- Li, P. et al. Infrared hyperbolic metasurface based on nanostructured van der Waals materials. Science 359, 892–896 (2018).
- 23. Li, P. et al. Collective near-field coupling and nonlocal phenomena in infrared-phononic metasurfaces for nano-light canalization. *Nat. Commun.* **11**, 3663 (2020).
- Tielrooij, K.-J. et al. Out-of-plane heat transfer in van der Waals stacks through electron-hyperbolic phonon coupling. Nat. Nanotechnol. 13, 41–46 (2018).
- Autore, M. et al. Boron nitride nanoresonators for phonon-enhanced molecular vibrational spectroscopy at the strong coupling limit. *Light Sci. Appl.* 7, 17172 (2018).
- Bylinkin, A. et al. Real-space observation of vibrational strong coupling between propagating phonon polaritons and organic molecules. *Nat. Photon.* 15, 197–202 (2021).
- Feres, F. H. et al. Sub-diffractional cavity modes of terahertz hyperbolic phonon polaritons in tin oxide. *Nat. Commun.* 12, 1995 (2021).
- Castilla, S. et al. Plasmonic antenna coupling to hyperbolic phonon-polaritons for sensitive and fast mid-infrared photodetection with graphene. *Nat. Commun.* 11, 4872 (2020).
- Kittel, C., McEuen, P. & McEuen, P. Introduction to Solid State Physics Vol. 8 (Wiley, 1996).
- 30. Landau, L. et al. *Electrodynamics of Continuous Media* Vol. 8 (Elsevier, 2013).
- Gillette, R. H. Calcium and cadmium tungstate as a scintillation counter crystal for gamma-ray detection. Rev. Sci. Instrum. 21, 294–301 (1950).
- 32. Mock, A., Korlacki, R., Knight, S. & Schubert, M. Anisotropy, phonon modes, and lattice anharmonicity from dielectric function tensor analysis of monoclinic cadmium tungstate. *Phys. Rev. B* **95**, 165202 (2017).

- Huber, A., Ocelic, N. & Hillenbrand, R. Local excitation and interference of surface phonon polaritons studied by near-field infrared microscopy. J. Microsc. 229, 389–395 (2008).
- 34. Lee, D. et al. Hyperbolic metamaterials: fusing artificial structures to natural 2D materials. *eLight* **2**, 1 (2022).

**Publisher's note** Springer Nature remains neutral with regard to jurisdictional claims in published maps and institutional affiliations.

Springer Nature or its licensor (e.g. a society or other partner) holds exclusive rights to this article under a publishing agreement with the author(s) or other rightsholder(s); author self-archiving of the accepted manuscript version of this article is solely governed by the terms of such publishing agreement and applicable law.

© The Author(s), under exclusive licence to Springer Nature Limited 2022

<sup>1</sup>Department of Electrical and Computer Engineering, National University of Singapore, Singapore, Singapore. <sup>2</sup>Wuhan National Laboratory for Optoelectronics and School of Optical and Electronic Information, Huazhong University of Science and Technology, Wuhan, China. <sup>3</sup>CAS Key Laboratory of Nanophotonic Materials and Devices, CAS Key Laboratory of Standardization and Measurement for Nanotechnology, CAS Center for Excellence in Nanoscience, National Center for Nanoscience and Technology, Beijing, China. <sup>4</sup>Institute of Materials Research and Engineering, Agency for Science, Technology and Research (A\*STAR), Singapore, Singapore. <sup>5</sup>NUS Graduate School, National University of Singapore, Singap

#### Methods

#### Permittivity of CdWO<sub>4</sub> crystal

The permittivity tensor of the  ${\rm CdWO_4}$  crystal in equation (1) is calculated by the Lorentz oscillator function with anharmonic broadening, where eight Lorentz oscillators were used for calculating each component.

$$\varepsilon_{xx} = \varepsilon_{xx,\infty} + \sum_{l=1}^{8} \varphi_l^{B_u} \cos^2 \gamma_l$$
 (2.1)

$$\varepsilon_{xy} = \varepsilon_{yx} = \varepsilon_{xy,\infty} + \sum_{l=1}^{8} \varphi_l^{B_u} \sin \gamma_l \cos \gamma_l$$
 (2.2)

$$\varepsilon_{yy} = \varepsilon_{yy,\infty} + \sum_{l=1}^{8} \varphi_l^{B_u} \sin^2 \gamma_l$$
 (2.3)

$$\varepsilon_{zz} = \varepsilon_{zz,\infty} + \sum_{i=1}^{7} \varphi_i^{A_u}$$
 (2.4)

$$\varphi_l = \frac{A_l^2 - i\omega \Gamma_l}{\omega_{\text{TO},l}^2 - \omega^2 - i\omega S_l}$$
 (2.5)

Here  $\varepsilon_{\infty}$  is the high-frequency permittivity for all the phonon modes along different directions where  $\varepsilon_{xx,\infty} = 4.460$ ,  $\varepsilon_{yy,\infty} = 4.810$ ,  $\varepsilon_{xy,\infty} = 0.086$  and  $\varepsilon_{zz,\infty} = 4.250$ ;  $\varphi_l$  describes the contributions of each optical phonon oscillator;  $A_l$ ,  $\omega_{\text{To},l}$ ,  $\Gamma_l$  and  $S_l$  denote the amplitude, transverse optical phonon frequency, harmonic broadening and transverse optical-mode broadening of the associated harmonic oscillators, respectively. Here  $\gamma_l$  is the unit-vector orientation of the eigendisplacement of the transverse optical mode. All the parameters of each harmonic oscillator are obtained from another work  $^{32}$ .

#### $\mathcal{M}$ factor for quantitative measurement of asymmetry

The  $\mathcal{M}$  factor as a quantity to measure the asymmetry is defined as

$$M(\theta) = \frac{\frac{1}{\varepsilon_{1}} \frac{\varepsilon_{xx}}{0} \varepsilon_{xy}}{\left| \frac{\varepsilon_{xx}}{0} \varepsilon_{yy} \right| - \left( \frac{\varepsilon_{1} \cos^{2}\theta + \varepsilon_{2} \sin^{2}\theta}{(\varepsilon_{1} - \varepsilon_{2}) \sin\theta \cos\theta} \right) \left| \frac{\varepsilon_{xy}}{0} \frac{\varepsilon_{yy}}{\varepsilon_{yy}} \right| - \left( \frac{\varepsilon_{1} - \varepsilon_{2}}{(\varepsilon_{1} - \varepsilon_{2}) \sin\theta \cos\theta} \frac{\varepsilon_{1} \sin^{2}\theta + \varepsilon_{2} \cos^{2}\theta}{(\varepsilon_{1} - \varepsilon_{2}) \sin\theta \cos\theta} \right) \left| \frac{\varepsilon_{xy}}{0} \frac{\varepsilon_{yy}}{\varepsilon_{yy}} \right| - \left( \frac{\varepsilon_{1} - \varepsilon_{2}}{(\varepsilon_{1} - \varepsilon_{2}) \sin\theta \cos\theta} \frac{\varepsilon_{1} \sin^{2}\theta + \varepsilon_{2} \cos^{2}\theta}{(\varepsilon_{1} - \varepsilon_{2}) \sin\theta \cos\theta} \right) \right|$$

where the matrix  $\begin{pmatrix} \varepsilon_1 & 0 \\ 0 & \varepsilon_2 \end{pmatrix}$  is the diagonalized matrix or eigenvalues of

 ${ig(rac{arepsilon_{xx} \ arepsilon_{xy}}{arepsilon_{xy} \ arepsilon_{yy}}ig)}$  using complex parameters. Hence, we have a mathematical

problem to minimize the value of  $\mathcal{M}=\min(M)$  with respect to real parameters  $\theta$ . A more detailed derivation is provided in Supplementary Section 1. For high-symmetry (hexagonal, orthorhombic and trigonal) crystals, one can mathematically prove that this quantity is zero. For monoclinic crystals, we can find that this is not always zero due to the non-diagonalizability of the permittivity tensor in real space. The larger the value of  $\mathcal{M}$ , the lower is the symmetry. In our study, for example, in Fig. 4, these values of  $\mathcal{M}$  are 0.0011, 0.0263 and 0.0808, respectively, which hence have increasingly low symmetry.

#### Numerical simulation

A finite element method using commercial software (COMSOL 5.6) is used to simulate the near-field distributions of polaritons launched by the vertical dipole. An electric dipole is placed 200 nm above the surface of the CdWO<sub>4</sub> crystal. The electric field distribution ( $E_z$ ) is recorded at 50 nm above the surface. A finite simulation range of 60  $\mu$ m  $\times$  60  $\mu$ m is mostly used in our simulations, with scattering boundary conditions. The energy has been decayed substantially from this range, and hence, the reflected field can be safely neglected. The simulation using larger areas is also used to confirm the field distribution.

#### Materials and fabrication

The CdWO $_4$  crystal with a polished (010) surface is obtained from a commercial company. The Au pattern on the crystal surface is fabricated using electron-beam lithography following a lift-off process. The electron-beam resist (ZEP520, Zeon) was spin coated on the sample and then baked for 10 min. A conductive polymer (AR-PC 5090.02, Allresist) was spin coated on the resist to prevent charge accumulation. The pattern of the resistor was drawn on the resist by electron-beam lithography (eLINE Plus). The sample was immersed in deionized water for 1 min to remove the conductive polymer and then immersed in a developing solution with developer N50 and IPA (isopropanol) (N50:IPA = 10:1, MACKLIN) for 1 min at 0 °C. A 100-nm-thick Au layer is deposited on the sample by electron-beam evaporation at 77 K refrigerated by liquid nitrogen. The deposition rate is fixed at 0.4 Å s<sup>-1</sup>. A quick lift-off process was conducted to define the Au pattern on the sample.

#### s-SNOM measurements

For the nanoimaging of polaritons in CdWO<sub>4</sub>, we used a commercial s-SNOM system (Neaspec) coupled with a tunable quantum cascade laser (Daylight Solutions) with an operation frequency from 950 to 860 cm<sup>-1</sup>. The infrared light illuminates a platinum-coated tip of an atomic force microscope operating in the tapping mode. The tip oscillates vertically at a frequency of  $\Omega \approx 270$  kHz and the oscillation amplitude is around 60 nm. The tip-scattered light is collected with a pseudo-heterodyne interferometer<sup>35</sup>. The background-free signal is demodulated at a higher harmonic of  $n\Omega$  ( $n \ge 2$ ), yielding images with near-field amplitude  $s_n$  and phase  $\varphi_n$ . Figure 3 show the images with amplitude  $s_2$ . The incident light is always oriented along the O1 axis of the CdWO<sub>4</sub> crystal during all the measurements.

## **Data availability**

All data are available in the Article or Supplementary Information.

### **References**

 Ocelic, N., Huber, A. & Hillenbrand, R. Pseudoheterodyne detection for background-free near-field spectroscopy. Appl. Phys. Lett. 89, 101124 (2006).

#### **Acknowledgements**

C.-W.Q. acknowledges support from the National Research Foundation, Prime Minister's Office, Singapore, under its Competitive Research Programme (CRP award NRF CRP22-2019-0006) and from the grant (A-0005947-16-00) from Advanced Research and Technology Innovation Centre (ARTIC). Q.D. acknowledges support from the National Natural Science Foundation of China (grant no. 51925203). D.H. acknowledges support from the National Natural Science Foundation of China (grant no. 52072083). J.D.C. acknowledges financial support from the US National Science Foundation (grant no. 2128240). J.W. acknowledges the Advanced Manufacturing and Engineering Young Individual Research Grant (AME YIRG grant no. A2084c170) and SERC Central Research Fund (CRF). P.L. acknowledges support from the National Natural Science Foundation of China (grant no. 62075070). W.M. acknowledges support from the Fundamental Research Funds for the Central Universities, HUST (grant no. 2022JYCXJJ009). A.A. and X.N. were supported by the Air Force Office of Scientific Research, the Office of Naval Research and the Simons Foundation.

## **Author contributions**

C.-W.Q, P.L. and A.A. conceived the idea. G.H. and W.M. performed the theory, simulation and design, with substantial input from C.-W.Q. and A.A. D.H. measured the sample with supervision by P.L. and Q.D. X.D.Z. fabricated the Au nanoantenna. G.H., W.M., X.L.Z., J.C., A.P., Q.D., A.A., P.L. and C.W. analysed the data, with input from all the authors. G.H.,

W.M. and D.H. wrote the manuscript with substantial contributions from all the others. C.-W.Q. oversaw the project.

## **Competing interests**

The authors declare no competing interests.

#### **Additional information**

**Supplementary information** The online version contains supplementary material available at https://doi.org/10.1038/s41565-022-01264-4.

**Correspondence and requests for materials** should be addressed to Qing Dai, Andrea Alù, Peining Li or Cheng-Wei Qiu.

**Peer review information** *Nature Nanotechnology* thanks the anonymous reviewers for their contribution to the peer review of this work.

**Reprints and permissions information** is available at www.nature.com/reprints.